ORIGINAL PAPER

Wear Induced Sub-surface Deformation Characteristics of a 26 Wt% Cr White Cast Iron Subjected to a Destabilization Heat Treatment

U. Pranav Nayak[1] · Florian Schäfer[3] · Frank Mücklich[1,2] · María Agustina Guitar[1]

Abstract

In the present work, the sub-surface microstructure of a heat treated and worn 26 wt% Cr white cast iron was investigated to gain better insight into the tribological behaviour of the material. The samples were destabilized at 980 °C for 0 (Q_0), 30 (Q_30) and 90 (Q_90) minutes followed by air cooling, and later subjected to dry-sliding linear reciprocating wear tests. The microstructural characterization of the area under the wear track was carried out using a combination of SEM, EDS and EBSD. Additionally, nanoindentation (NI) measurements were used to corroborate the mechanical behaviour with the microstructural observations. EBSD and NI measurements indicated that the matrix area underneath the wear track in Q_0 had undergone significant plastic deformation resulting in a drastic increase in hardness, whereas no such phenomena was observed in the Q_90. This was attributable to the relatively high amount of retained austenite in the former and a predominately martensitic matrix in the latter. Moreover, the large M_7C_3 eutectic carbides were less cracked in the destabilized samples compared to the as-cast sample owing to the presence of martensite and dispersed secondary carbides, leading to an increased matrix load-bearing capacity. These factors led to the destabilized samples showing a lower wear rate compared to the as-cast sample, and the Q_0 showing the best wear resistance amongst all the samples.

Keywords High chromium cast iron · Destabilization heat treatment · Sub-surface microstructure · Nanoindentation · Retained austenite · Wear rate

1 Introduction

Considering the money and energy that is being spent on overcoming tribological related issues during the operation run time, it is imperative to develop better wear-resistant materials by understanding the underlying wear mechanisms [1–3]. The dispersion of hard carbides in a supportive, modifiable matrix makes high chromium cast iron (HCCI) alloys viable candidates for wear-resistant applications, particularly in the mining and mineral industry [4–7]. By employing suitable heat treatment (HT) procedures such as destabilization and/or sub-critical treatments, the matrix can be accordingly modified [8, 9]. Moreover, the type and nature of the secondary carbides (SC) which precipitate during the destabilization HT are highly dependent on the Cr/C ratio, in addition to the HT parameters [4, 10, 11].

The influence of heat treatment conditions on the wear properties of HCCI's has been evaluated by several studies, where a strong interdependence between the microstructural characteristics and wear resistance was observed [8, 9, 12–15]. Moreover, as the maximum stress is experienced at the centre of the wear track, making transverse cuts across the entirety of the track would be beneficial [16, 17]. This will help in gaining a better insight into the tribological behaviour of the material aiding in further development [18, 19]. Therefore, in addition to the wear-induced microstructural modifications on the sample's surface, examining the region under the wear track is crucial. Microstructural characterization was previously done to assess the deformation behaviour at the sub-surface level on copper and iron [16, 20, 21]. Furthermore, evaluating the sub-surface microstructure greatly benefited in understanding the tribological behaviour of certain HCCI alloys as well [22–24].

✉ U. Pranav Nayak
  pranav.nayak@uni-saarland.de

1 Department of Materials Science, Saarland University, Campus D3.3, 66123 Saarbrücken, Germany

2 Materials Engineering Center Saarland (MECS), Campus D3.3, 66123 Saarbrücken, Germany

3 Department of Materials Science and Methods, Saarland University, Campus D2.3, Saarbrücken, Germany

Penagos et al., [22] investigated the influence of structure refinement on the wear resistance of a hypoeutectic HCCI alloy that was casted in a single mould such that a fine to coarse M_7C_3 carbide gradient existed in the microstructure. Upon analysing the sub-surface, they observed that the microstructure consisting of coarse M_7C_3 carbides showed sub-critical cracking and no fracture, compared to its finer counterpart. This was reflected in the abrasion tests wherein the microstructure with refined carbides showed a lower abrasion resistance compared to the coarser carbides. In fact, the larger M_7C_3 carbides were acting as a barrier to the abrasive grit resulting in a higher wear resistance.

On the other hand, Matsuo et al., [23] studied the wear behaviour of three different spray formed HCCI alloys and compared them to their respective conventionally cast counterparts. The analysis of the sub-surface shed further light on the improved wear resistance of the spray-formed HCCI over the conventionally cast HCCI. They observed that the matrix and the carbide had deeper cracks underneath the wear track in the conventionally cast alloy compared to the spray-formed. This was attributed the spray-formed HCCI possessing a finer and more homogeneously distributed M_7C_3 carbides, and a well-balanced matrix consisting of austenite and martensite.

The above two investigations clearly depict the ambivalence between them, where one study claims having a finer carbide distribution is better for wear, whereas the other study mentions the opposite. This just elucidates the complexity between the microstructure and wear relationship, and the dependence on the conditions under which the tests were undertaken. Owing to the 'composite' like behaviour in HCCIs, the overall tribological behaviour is not an inherent property but a synergistic contribution between the hard carbides and the matrix that engulfs it [3, 25, 26]. In addition to the characteristics of the hard M_7C_3 carbides, the degree to which the matrix provides the necessary mechanical support is crucial [27, 28]. Furthermore, depending on the applicability, the stereological characteristics of the secondary carbides may also have an influence on the overall behaviour [29, 30].

Previously, a destabilization HT was experimentally conducted on as-cast (AC) 26 wt% Cr white cast iron samples wherein they were heated to 980 °C for various times ranging from 0 to 90 min, followed by air cooling. They were later subjected to dry-sliding linear reciprocating tribological tests in order to derive a mutual relationship between the wear rate and the varying microstructural characteristics. Subsequently, it was observed that: (1) all the HTed samples showed a lower wear rate compared to the AC, and (2) amongst the HTed samples, the sample with the lowest surface matrix hardness showed the best wear resistance. These changes were attributed to the varying fractions of the microstructural constituents and their respective distribution within the destabilized microstructure [31].

The main objective of the present work is to gain a better understanding of the tribological behaviour of the destabilized samples by investigating the area directly underneath the wear track. Microstructural characterization of the sub-surface was carried out using scanning electron microscopy (SEM) in conjunction with electron backscattered diffraction (EBSD). Finally, nanoindentation (NI) measurements were performed around the vicinity of the wear track with increasing cross-sectional depth to corroborate the deformation behaviour with the destabilized microstructure.

2 Experimental Methodology

An as-cast HCCI alloy (~ Cr: 26.6 wt%; C: 2.5 wt%; Mn: 0.66 wt%; Mo: 0.24 wt%; Ni: 0.26 wt%; Si: 0.37 wt%; Fe: Bal.) measuring $20 \times 20 \times 10$ mm was subjected to a destabilization HT at 980 °C (1253 K) for 0 (Q_0), 30 (Q_30) and 90 (Q_90) minutes, followed by air cooling. The increase in the destabilization holding time resulted in variable fractions of the micro-constituents i.e., retained austenite (RA), martensite and SC, in addition to the relatively unchanged M_7C_3 eutectic carbides (EC), as previously described in [31]. Dry-sliding linear reciprocating tribological tests were later performed on the HTed samples using 3 mm alumina (Al_2O_3) balls (99.00–99.99% purity; Grade GD28) as the sliding counter-body.

The surface and sub-surface underneath the wear track were protected with an electrolytically deposited Ni coating and then mechanically sectioned. Further specifics concerning the Ni electrodeposition process are elaborated in [32]. Subsequently, a scratch-free, mirror-polished surface of the transverse section was obtained by following the metallographic protocol as described in [33]. Microstructural characterization of the sub-surface was carried out with a Thermo-Fisher Helios™ G4 PFIB (Plasma Focused-Ion Beam) CXe DualBeam™ FIB/SEM which was operated at an accelerated voltage of 5–15 kV and a beam current of 1.6 nA. Additionally, energy-dispersive X-ray spectroscopy (EDS) was used to chemically map the cross section containing both the sub-surface and the Ni coating. The SEM micrographs were taken in backscattered mode for a better contrast between the different phases. The microstructural constituents are colour arrow coded throughout the paper according to the following terminology:

Austenite (γ): Red arrow pointing downwards.
Martensite (α'): Green arrow pointing upwards.
M_7C_3 carbide (EC): Yellow arrow pointing right.
$M_{23}C_6$ carbide (SC): Blue arrow pointing left.

EBSD was employed to investigate the strain distribution and local deformation around the regions underneath the wear track. The measurements were performed at an acceleration voltage of 20 kV and a beam current of 11 nA using the FEI Helios™ Nanolab 600 field emission SEM (FE-SEM) workstation equipped with an EDAX Hikari EBSD camera. Furthermore, the orientational variation of the matrix region with increasing cross-sectional depth was obtained by grain reference orientation deviation (GROD) maps and performing misorientation profile (MP) analysis. The GROD was performed by considering a 3rd degree neighbour owing to the very small step size (50 nm) used. The EBSD data was analysed using the Orientation Imaging Microscopy (OIM™ v. 7) Data Analysis software by EDAX Corporation.

NI measurements were carried out using a Hysitron TI900 TriboIndenter® Nanomechanical Testing System with nanoDMA upgrade with a Berkovich 142.3°, 3-sided pyramidal indenter. Open-loop intrinsic load-controlled tests were performed with a loading rate of 1 mN/s and a peak load of 3 mN. To account for a potential drift, the drift rate was measured at a pre-load of 2 μN for 20 s and the results were drift-corrected. During the test, drift was checked by additional hold segments of 2 s at 100 μN before and after applying the peak load. Datasets that suffer from drift were excluded from the subsequent evaluation. To account for creep, the peak load was held for 2 s. The values of the nanoindentation hardness (H) and the reduced indentation modulus (E) were obtained after analysing the NI curves employing the Oliver-Pharr method [34, 35]. To achieve a good spatial resolution and to reduce the influence of sub-surface in-depth microstructural and mechanical gradients, a small indentation depth of less than 100 nm was used. Therefore, special attention was laid on the probe calibration. The validity of the probe calibration was guaranteed by an almost constant reduced indentation modulus over the indentation depth, measured using nanoDMA, for all indents included in the subsequent evaluation. At least 100 indentations (10 by 10) were performed in a regularly spaced grid directly underneath the wear track, and also away from the wear track. Moreover, to avoid any overlapping effect, a distance of 3 μm was maintained between two indents regarding a maximum indent diameter below 1 μm.

3 Results and Discussion

In an own previous study, the influence of increasing the destabilization holding time on the microstructural evolution and tribological behaviour of the same sample was investigated [31]. In the AC sample, the microstructure primarily consisted of an austenitic matrix and dispersed M_7C_3 EC with the martensite sandwiched at the interface. The destabilization heat treatment resulted in the precipitation of fine $M_{23}C_6$ type SC within the matrix, whereas the EC remained relatively immune. Finally, the extent to which the austenite had transformed to martensite during cooling varied as a function of holding time. Table 1 briefly summarizes the quantification of the microstructural constituents such as RA, secondary carbide size and carbide volume fraction (CVF), and the surface matrix hardness.

It is observed from Table 1 that increasing the holding time during destabilization results in a reduction of the amount of RA and a corresponding increase in the matrix hardness. Moreover, it was seen that the volume fraction of SC was statistically comparable in the samples destabilized for 0 and 90 min, although the average size almost doubled in the latter. The mutual dependence of the wear rate (WR) $(mm^3\ N^{-1}\ mm^{-1})$ on the amount of retained austenite and the matrix hardness is graphically represented in Fig. 1. Additionally, representative BSE SEM micrographs of the AC, Q_0 and Q_90 samples are shown. In the Q_0 sample, the central part of the matrix is austenite (retained austenite) while little to no austenite is seen in the Q_90 sample's matrix. Although the microstructural constituents of the destabilized samples were identical, the differences in their amounts and distribution had a consequence on the final tribological properties of the alloy, as previously discussed in [31].

Figure 1 indicates that all the destabilized samples showed a lower WR compared to the AC sample, and a harder matrix did not necessarily guarantee a better wear resistance. Interestingly, the Q_0 sample displayed the lowest WR (i.e., highest wear resistance) despite showing the smallest increase in the matrix hardness compared to the AC. This was attributed to a favourable distribution of the RA (~ 10%) and SC volume fraction (~ 5%) in combination with a harder martensitic matrix.

In order to gain a better understanding of the tribological behaviour of the destabilized samples, it is imperative to characterize the sub-surface microstructure. Therefore, by observing the deformation characteristics of the surface directly underneath the wear track, more insight could be gained as to why the Q_0 sample showed the highest wear resistance.

Table 1 Quantification of retained austenite, SC characteristics and matrix hardness in the as-cast and destabilized samples [31]

Sample	RA (%)	SC CVF (%)	SC size (μm²)	Matrix hardness (HV0.1)
As-cast	58.1	–	–	347 ± 24
Q_0	10.2	5 ± 0.15	0.023 ± 0.030	412 ± 31
Q_30	7.1	3.15 ± 0.81	0.028 ± 0.039	759 ± 22
Q_90	5.1	5.77 ± 0.99	0.041 ± 0.073	775 ± 33

Fig. 1 The dependence of WR on the amount of RA and the matrix hardness in all samples. Representative BSE SEM micrographs of AC, Q_0 and Q_90 samples are also presented. The various microstructural constituents are colour-arrow coded for reference (Color figure online)
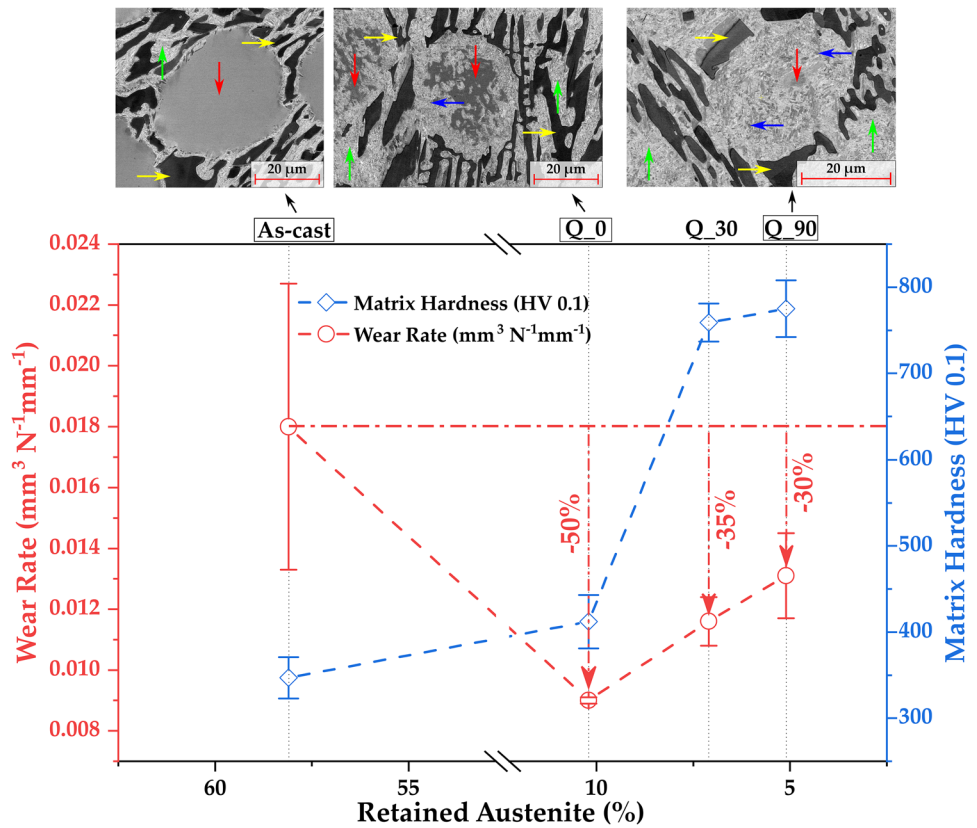
3.1 Microstructural Characterization of the Sub-surface

Figure 2 represents the BSE SEM micrographs of the transverse section of the AC, Q_30 and Q_90 samples. In all cases, the Ni coating was uniform and adherent across the entire surface and was successful in protecting the worn surface during the polishing and the subsequent mechanical sectioning. Figure 2a.1 and a.2 indicate the transverse section of the unworn and the worn surface in the AC sample, respectively. Figure 2a.3 is a magnified region of the dashed-blue enclosure in Fig. 2a.2. Comparing Fig. 2a.1 with a.2, it was seen that the EC underneath the wear track had undergone cracking, primarily perpendicular to the sliding direction. Moreover, the Ni coating was successful in preventing the cracked carbides from ejecting out by acting as an anchor between the cracks, as shown in Fig. 2a.3.

Figure 2b.2 represents the EDS concentration maps of Ni and Cr of the SEM micrograph presented in Fig. 2b.1. The EDS spectra for the whole region is presented in Fig. 2b.3 and the distribution of the SC can be visualized from the Cr map. Figure 2c.1 indicates the BSE SEM micrograph of the transverse section of the Q_90 sample containing the wear track with the inset representing a magnified image of the cracked EC. Similar to the AC, the carbide had cracked perpendicularly to the sliding

direction, and it is worth to note that the crack had terminated at the edge of the carbide. This was attributable to the variation in the crystal structure and hardness between the EC and the matrix [36]. Moreover, the inset clearly shows that some transformation had taken place (indicated by the dashed-green enclosure) as visualized by the contrast difference. This was also observed in other studies [37–39] and could be attributed to the destabilization process. The EDS concentration map (Fig. 2c.2) clearly shows the distribution of Ni and Cr within the sample. The EDS line spectra in Fig. 2c.3 tracing the line marked in Fig. 2c.2 indicates the abundance of Cr and Fe as it traces the carbide or the matrix, respectively.

The inverted BSE SEM micrograph of the area underneath the wear track, where the EBSD measurements were carried out, is indicated in Fig. 3a.1. Figure 3a.2 and a.3 represents the phase map and the IPF map of the entire region. Figure 3a.4 represents the GROD map of only the austenitic region under the wear track. Furthermore, the orientational variation across the entire austenite grain was visualized by calculating the point-to-point and point-to-origin misorientation profile chart, as graphically represented in Fig. 3a.5. The point O (as marked in Fig. 3a.4) was selected as the origin point, as it lies away from the immediate wear surface, and the MP measurements were carried out proceeding closer towards the deformed austenite. The point-to-origin
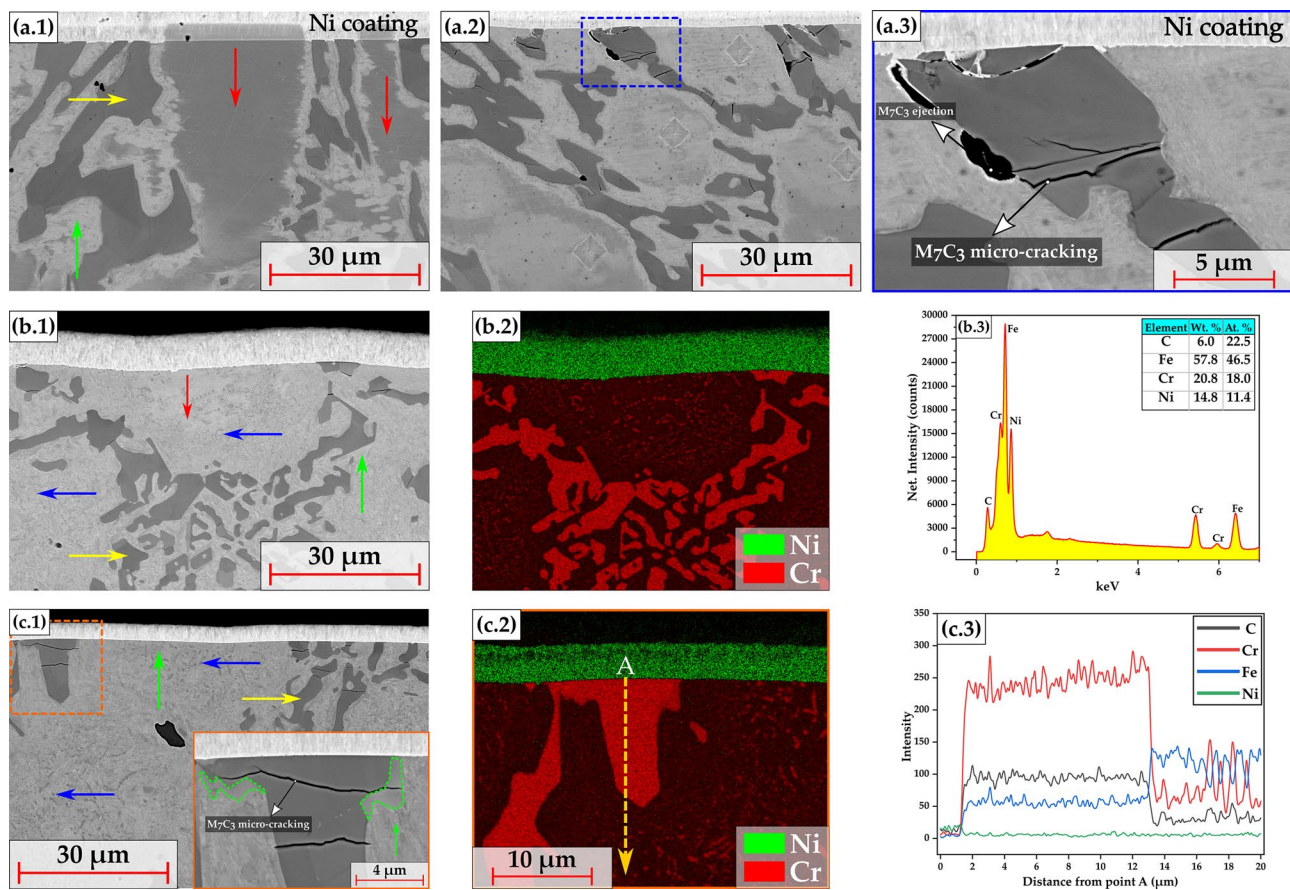
Fig. 2 Representative BSE SEM micrographs of the transverse section of the AC sample **a.1** away from the wear track, **a.2** underneath the wear track, **a.3** magnified view of the dashed-blue enclosure in **a.2** depicting the cracking of the EC carbide. **b.1** representative BSE SEM micrographs of the transverse section of the Q_30 sample underneath the wear track, **b.2** overlayed EDS concentration maps of Ni and Cr, **b.3** resulting EDS scan with the semi-quantitative analysis of the phases. **c.1** representative BSE SEM micrograph of the transverse section of the Q_90 sample underneath the wear track. The inset in **c.1** is a magnified view of the dashed-orange enclosure indicating the EC carbide micro-cracking, and the partial transformation, represented by the dashed-green enclosure. **c.2** overlayed EDS concentration maps of Ni and Cr and **c.3** EDS line scan result with A as the starting point [marked in **c.2**] (Color figure online)

plot indicates a maximum gradient of about 11° between the undeformed and deformed austenite region.

Similarly, EBSD measurements were also carried out in the unworn region across the wear track as represented in the dashed enclosure in Fig. 3b.1. The phase maps and IPF maps are presented in Fig. 3b.2 and b.3, respectively. The GROD map in Fig. 3b.4 clearly shows that the austenite under the coating did not experience any deformation. This is also indicative that the mechanical sectioning and polishing had no influence on the deformation of the cross section, and the deformed regions underneath the wear track were a consequence of the tribological test in itself.

Analogous to the Q_0 sample, similar EBSD measurements were carried out on the Q_90 sample. Figure 4a.1 and Fig. 4b.1 represents the SEM micrographs of the region directly underneath the wear track, and about 350 μm below the Ni coating, respectively. The dashed-yellow and dashed-red enclosures represent the areas where the EBSD

measurements were carried out. Comparing the phase maps (Fig. 4a.2 and b.2), IPF (Fig. 4a.3 and b.3) and GROD maps (Fig. 4a.4 and b.4) amongst the two regions, no major differences were seen indicating that the region immediately underneath the wear track was not subjected to deformation as in the case of the Q_0 sample. This was attributed to the predominately martensitic matrix in the Q_90 sample which is harder compared to its austenite counterpart. The presence of relatively larger amount of austenite in the Q_0 sample results in its plastic deformation under the wear track leading to the gradient as observed in Fig. 3a.4.

Figure 5a is indicative of the inverted SEM micrograph on which the EBSD measurements were done, with Fig. 5b representing the phase map. The orientational variation within the M_7C_3 carbide was visualized by overlaying the IQ map with the GROD map as represented in Fig. 5c. The propagation and termination of the cracks can be clearly seen, and the area immediately underneath the wear track
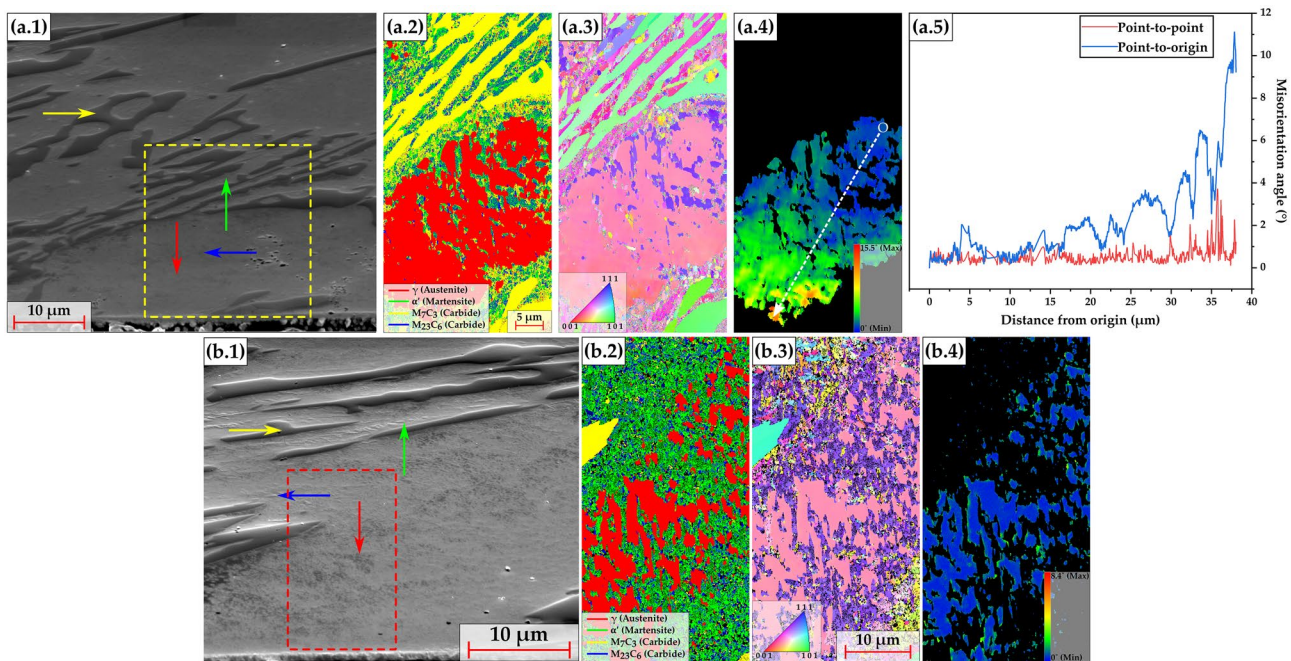
Fig. 3 Representative inverted SEM micrographs of the Q_0 sample **a.1** underneath the wear track and **b.1** away from the wear track. The dashed-yellow (in **a.1**) and the dashed-red enclosures (in **b.1**) indicate the region where the EBSD measurements were carried out. **a.2**, **a.3**, **a.4** represent the phase map, IPF, and GROD map for the austenite at the worn surface, respectively, whereas **b.2**, **b.3** and **b.4** represents the same for the unworn surface. **a.5** MP chart with O as the starting point and proceeding towards the worn region, as indicated in **a.4** (Color figure online)

and the dashed-white enclosed region had undergone deformation due to the compressive stress acting on the carbide. Indeed, the orientational tolerance of the carbide before it underwent cracking was very low as it is unable to plastically deform. Nevertheless, by implementing EBSD, these minute changes within the carbide can be visualized and a better understanding can be obtained.

3.2 Nanoindentation Measurements of the Sub-surface

Figures 6 and 7 represent the NI grid measurements that were performed on the transverse section containing the wear track in the Q_0 and Q_90 sample, respectively. The dashed enclosure in Fig. 6a represents the area where the NI mapping took place and Fig. 6b shows the hardness contour plot that was obtained after performing the necessary corrections (following the Oliver and Pharr method). From the contour plot, it can be visualized that the area immediately under the wear track was harder as opposed to 20 μm below. Moreover, the EC and the areas surrounding them were harder as observed from the contour plot. A heat map of the reduced elastic modulus is represented in Fig. 6c mimicking the trend shown from the contour plot. Comparing Fig. 6a to the EBSD Phase Map in Fig. 3a.2, correlations can be drawn that the area immediate

underneath the wear track was a mixture of martensite plus the dispersed secondary carbides. Notwithstanding the plastic deformability of the austenite which reduced with increasing cross-sectional depth, the hardness contour plot reflects the different regions under the wear track. The solid white line enclosure basically represents the dispersed SC plus the martensite, whereas the dashed-white enclosure represents the hardness range < 7.5 GPa, where the austenite (both deformed and undeformed) falls in.

As far as the Q_90 sample is concerned, not a lot of variation in hardness is seen immediately below the track, as observed from Fig. 7b. Compared to Q_0, the mean value of the matrix hardness is higher (darker shade of blue) owing to the presence of a martensitic matrix, larger-sized SC, and a low content of retained austenite (~5%). The NI measurements corroborate the observations made from the EBSD measurements, i.e. the matrix area immediately beneath the wear track was not subjected to deformation. The notion that the matrix hardness within the Q_90 sample remains mainly invariant is further bolstered by observing the histogram of the NI measurements which were carried out immediately underneath and at ~350 μm below the wear track. In both cases, the two peaks in the graph represent the matrix and the eutectic carbides, with the mean value of the matrix centred at around 8 GPa. The load used in this study was below the threshold for
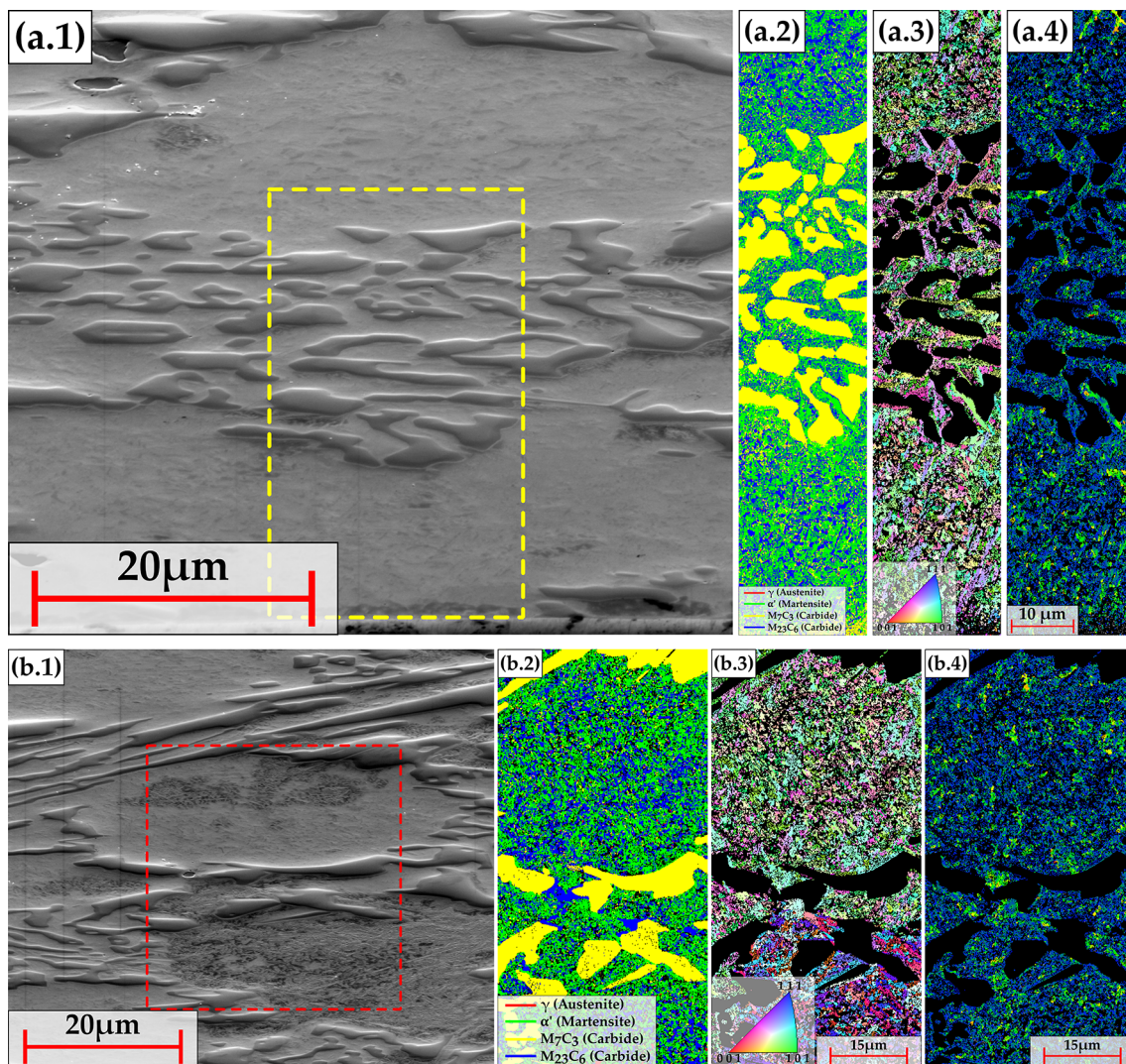
Fig. 4 Representative inverted SEM micrographs of the Q_90 sample **a.1** underneath the wear track and **b.1** 350 μm below the wear track. The dashed-yellow (in **a.1**) and the dashed-red enclosures (in **b.1**) indicate the region where the EBSD measurements were carried out. (**a.2**), (**a.3**) and (**a.4**) represent the phase map, IPF and GROD map at the worn surface, respectively, whereas (**b.2**), (**b.3**) and (**b.4**) represents the same for the unworn surface (Color figure online)

martensite to plastically deform. Nevertheless, comparing the hardness contour plots with the respective EBSD mappings, the changes in the matrix hardness within the Q_0 sample can be observed.

Finally, the variation of the matrix hardness with increasing cross-sectional depth for the destabilized samples is graphically represented in Fig. 8. Additionally, the average hardness value for austenite (γ) and martensite (α') for the AC sample is also indicated. Amongst the Q_0 and the Q_90 sample, major variation in the hardness can be seen going away from the wear track. In the Q_0 sample, the region immediately below the wear track showed the highest hardness amongst all the samples. This increase was not only attributed to the plastic deformation of the austenite alone, but also the presence of the martensite and the SC located

primarily around the periphery of matrix. This combination resulted in a high hardness for the Q_0 sample below the wear surface. Additionally, the SC precipitation and the alloy distribution that takes place during the destabilization HT results in the final remaining austenite to be further enriched in carbon and other elements, increasing its inherent hardness. This was reflected in the NI measurements wherein the AC austenite had a hardness of about 4.7 GPa, whereas in the Q_0, it was 5.3 GPa. The Q_90 sample maintained its hardness throughout the measured depth (up to ~350 μm) indicating that no increase in hardness underneath the wear track was observed. Previously, a homogeneity factor termed the coefficient of variation (COV) was introduced to determine the uniformity in the SC dispersion in the destabilized samples wherein a lower COV value
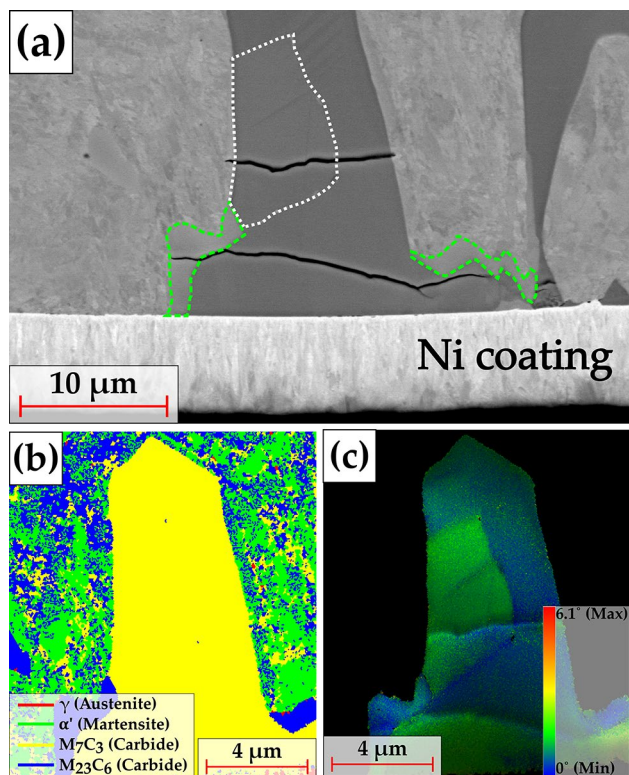
Fig. 5 a Representative inverted SEM micrograph of the Q_90 sample under the wear track indicating the cracked M_7C_3 EC. The dashed-green enclosures at the periphery indicate the partial transformation to $M_{23}C_6$. **b** EBSD phase map and **c** IQ + GROD map of the large EC (Color figure online)

implied a higher homogeneity. In the case of Q_0, the COV was around 40%, whereas in the Q_90 sample it was almost 50% [31]. The increased homogeneity in the Q_0 sample combined with its small-sized carbides, primarily dispersed around the periphery, led to the region below the wear track to show such an increase in the hardness.

Classical wear theories emphasize on the hardness as the defining property of a surface's wear resistance [3, 40]. The

ratio of H/E is widely considered to be a valuable parameter in determining the elastic behaviour of a surface contact, as popularized by Oberle [41]. This parameter has also been used in other studies to gain an idea of the wear resistance based on the NI measurements [42–44]. It is worth to note that the higher the H/E ratio, the higher the wear resistance. Figure 9 represents the H/E histograms for all the samples (AC and destabilized) including their distribution curves and rug plots.

The two distinct peaks from the distribution curves for every sample represent the matrix and the carbide H/E values, analogous to the hardness histogram curve in Fig. 7d. From the graph, two definite separations can be made based on the mean matrix H/E ratio (the 1st peak of the curve) wherein the mean H/E value of the AC is slightly lower compared to the destabilized one. Therefore, one may hypothesize that the wear resistance of the AC is lower than the destabilized ones, which was true in our case. Nevertheless, it should be treated with caution as the graph does not consider the complexities and the varying parameters that the tribological test may include, i.e. the atmospheric conditions, the counter-body used etc., in addition to the dynamic microstructural changes that take place during the sliding wear such as phase transformations, plastic deformation of the austenite etc. [45]. Although the graph considers the variation in the hardness between the austenite and martensite (as evident from the AC and destabilized samples), amongst the destabilized samples, further factors come into play, such as the stereological characteristics of the secondary carbides. As mentioned earlier, despite having the same micro-constituents, their amounts and distribution play a major role in determining the final tribological properties. Even if no major conclusions can be drawn between the destabilized samples solely from this graph, by combining the information obtained from microstructural characterization with the NI measurements, the differences in the tribological behaviour can be explained.
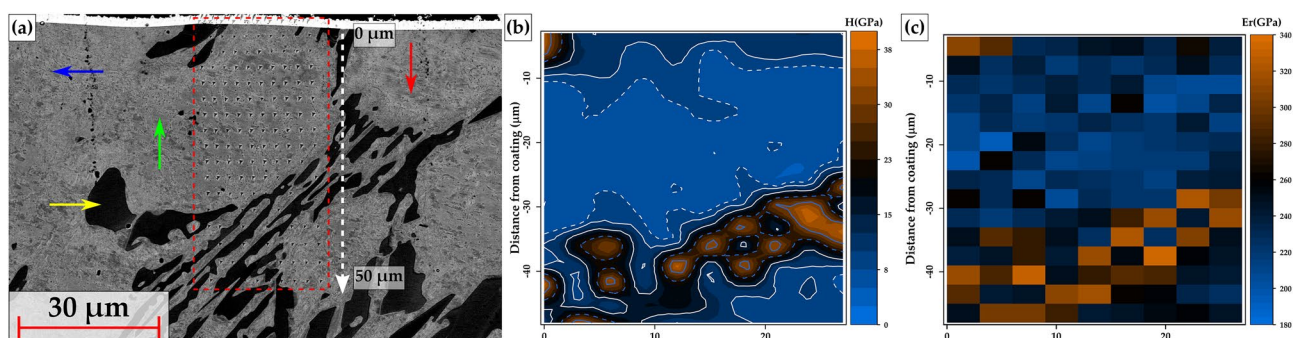

Fig. 6 a Representative BSE SEM micrograph of the transverse section of the Q_0 sample with the dashed-red enclosure indicating the region where the NI grid measurements were carried out, **b** hardness contour plot and **c** heat map of the reduced elastic modulus of the mapped region (Color figure online)
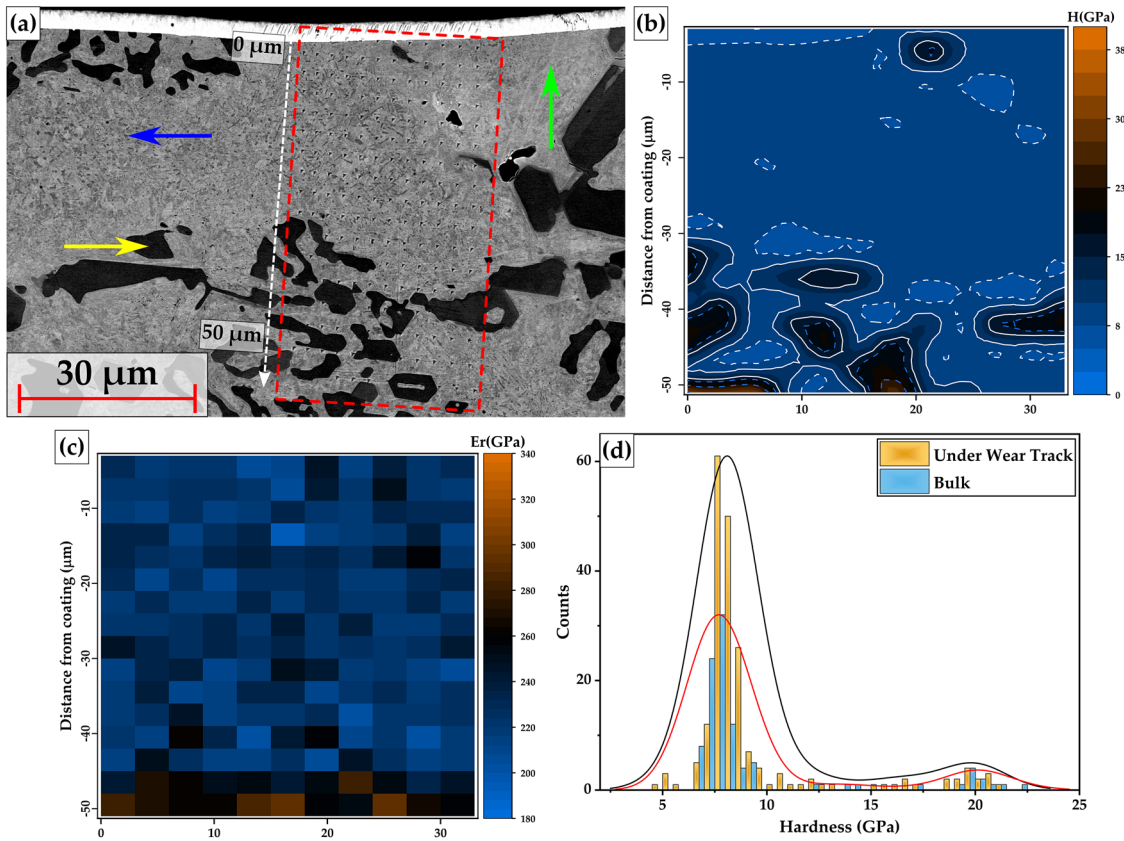
Fig. 7 **a** Representative BSE SEM micrograph of the transverse section of the Q_90 sample with the dashed-red enclosure indicating the region where the NI grid measurements were carried out, **b** hardness contour plot, **c** heat map of the reduced elastic modulus of the mapped region and **d** histogram of the hardness measurements with the respective distribution curves carried out in the region underneath and 350 µm below the wear track (Color figure online)
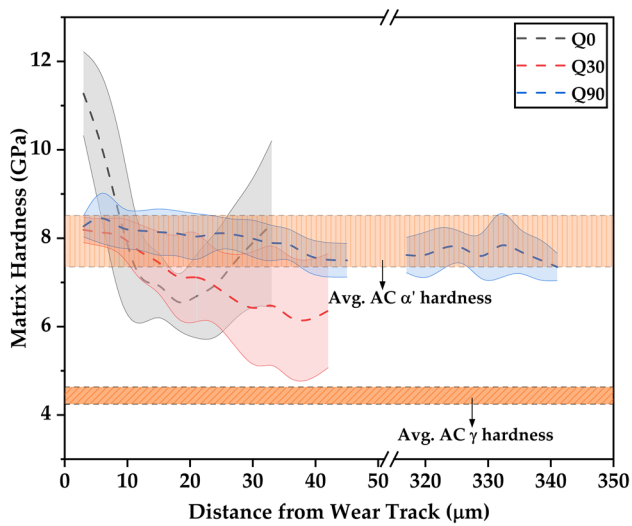

Fig. 8 Variation of matrix hardness with increasing cross-sectional depth in the destabilized samples. The average austenite and martensite hardness in the AC sample is also indicated
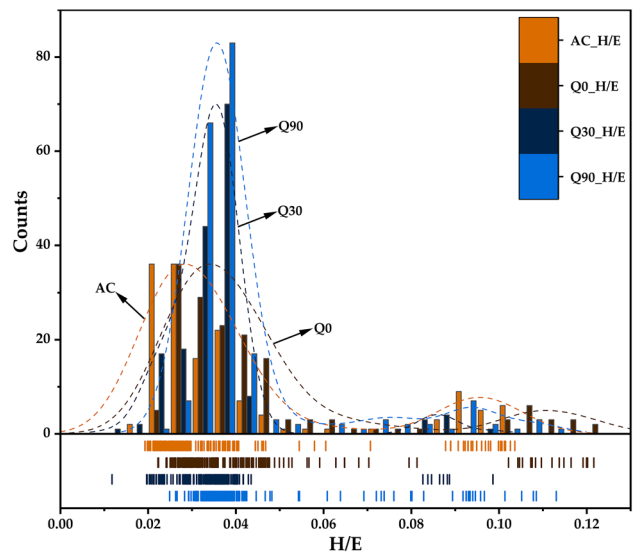
Fig. 9 Histogram of the measured H/E values for all the samples with the respective distribution curves and rug plots

Another observation was the increased prevalence in the cracking of the large EC in the AC sample compared to the destabilized samples. Although it was hypothesized in our previous work during the examination of the wear surface, investigating the sub-surface shed further light on this matter. In the destabilized samples, the presence of a predominately martensitic matrix and the dispersion of SC improves the load-bearing capacity in distributing the load so that the EC alone do not have to bear the brunt [22, 46, 47]. In the AC sample, only a small fraction of the microstructure is martensitic, which are primarily located at the interface between the EC and the austenite. As a result, the EC will succumb to cracking and eventual ejection during the tribological tests. The cracking of the large EC will further accelerate the wear rate and eventually lower the wear resistance.

4 Conclusions

In the present work, the sub-surface microstructure of a destabilized and worn 26 wt% Cr white cast iron was investigated to gain better insight into the tribological behaviour of the material, and the following conclusions were drawn.

- In the Q_0 sample, EBSD measurements indicated that the austenite region directly underneath the wear track had deformed and this was also corroborated with NI measurements.
- The presence of a predominately martensitic matrix combined with the dispersed SC in the Q_90 sample did not cause a substantial increase in the hardness under the wear track compared to the bulk.
- Despite the Q_0 having the lowest increase in matrix surface hardness amongst the HTed samples, it showed the highest sub-surface hardness. This was attributed to the presence of small-sized, homogeneously distributed SC around the periphery combined with the martensite, and the relatively higher amount of RA, which underwent plastic deformation.
- In all the destabilized samples, the presence of martensite and the dispersion of SC around the larger M_7C_3 EC led to an improvement in the load-bearing capacity, thereby reducing the tendency for EC micro-fracture, compared to the AC.

Declarations

References

1. Holmberg, K., Kivikytö-Reponen, P., Härkisaari, P., Valtonen, K., Erdemir, A.: Global energy consumption due to friction and wear in the mining industry. Tribol. Int. **115**, 116–139 (2017). https://doi.org/10.1016/j.triboint.2017.05.010

2. Watson, J.D., Mutton, P.J., Sare, I.R.: Abrasive wear of white cast irons. Metals Forum. **3**, 74–88 (1980)

3. Zum Gahr, K.H., Doane, D.V.: Optimizing fracture toughness and abrasion resistance in white cast irons. Metall. Trans. A. **11**, 613–620 (1980). https://doi.org/10.1007/BF02670698

4. Tabrett, C.P., Sare, I.R., Ghomashchi, M.R.: Microstructure-property relationships in high chromium white iron alloys. Int. Mater. Rev. **41**, 59–82 (1996). https://doi.org/10.1179/095066096790326075

5. Karantzalis, E., Lekatou, A., Mavros, H.: Microstructure and properties of high chromium cast irons: effect of heat treatments and alloying additions. Int. J. Cast Met. Res. **22**, 448–456 (2009). https://doi.org/10.1179/174313309X436637

6. Maratray, F.: Choice of appropriate compositions for chromium-molybdenum white irons. AFS Trans. **79**, 121–124 (1971)

7. Nayak, U.P., Guitar, M.A., Mücklich, F.: A comparative study on the influence of chromium on the phase fraction and elemental distribution in as-cast high chromium cast irons: Simulation vs. experimentation. Metals (Basel). (2020). https://doi.org/10.3390/met10010030

8. Karantzalis, A.E., Lekatou, A., Mavros, H.: Microstructural modifications of as-cast high-chromium white iron by heat treatment. J. Mater. Eng. Perform. **18**, 174–181 (2009). https://doi.org/10.1007/s11665-008-9285-6

9. Guitar, M.A., Suárez, S., Prat, O., Duarte Guigou, M., Gari, V., Pereira, G., Mücklich, F.: High chromium cast irons: destabilized-subcritical secondary carbide precipitation and its effect on hardness and wear properties. J. Mater. Eng. Perform. (2018). https://doi.org/10.1007/s11665-018-3347-1

10. Wiengmoon, A., Chairuangsri, T., Pearce, J.T.H.: A microstructural study of destabilised 30wt%Cr-2.3wt%C high chromium cast iron. ISIJ Int. **44**, 396–403 (2004). https://doi.org/10.2355/isijinternational.44.396

11. Powell, G.L.F., Laird, G.: Structure, nucleation, growth and morphology of secondary carbides in high chromium and Cr-Ni white cast irons. J. Mater. Sci. **27**, 29–35 (1992). https://doi.org/10.1007/BF02403640

12. Guitar, M.A., Nayak, U.P., Britz, D., Mücklich, F.: The effect of thermal processing and chemical composition on secondary carbide precipitation and hardness in high-chromium cast irons. Int. J. Metalcast. **14**, 755–765 (2020). https://doi.org/10.1007/s40962-020-00407-4

13. Gasan, H., Erturk, F.: Effects of a destabilization heat treatment on the microstructure and abrasive wear behavior of high-chromium white cast iron investigated using different characterization techniques. Metall. Mater. Trans. A. **44**, 4993–5005 (2013). https://doi.org/10.1007/s11661-013-1851-3

14. Kibble, K.A., Pearce, J.T.H.: Influence of heat treatment on the microstructure and hardness of 19% high-chromium cast irons. Cast Met. **6**, 9–15 (1993). https://doi.org/10.1080/09534962.1993.11819121

15. Tabrett, C.P., Sare, I.R.: Effect of high temperature and sub-ambient treatments on the matrix structure and abrasion resistance of a high-chromium white iron. Scr. Mater. **38**, 1747–1753 (1998). https://doi.org/10.1016/S1359-6462(98)00118-3

16. Ruff, A.W.: Deformation studies at sliding wear tracks in iron. Wear **40**, 59–74 (1976). https://doi.org/10.1016/0043-1648(76)90018-1

17. Grützmacher, P.G., Rammacher, S., Rathmann, D., Motz, C., Mücklich, F., Suarez, S.: Interplay between microstructural evolution and tribo-chemistry during dry sliding of metals. Friction. **7**, 637–650 (2019). https://doi.org/10.1007/s40544-019-0259-5

18. Mercado, V.H., Mejía, I., Bedolla-Jacuinde, A.: Effect of load and sliding rate on the wear behavior of Ti-containing TWIP steel. J. Mater. Eng. Perform. **26**, 2213–2225 (2017). https://doi.org/10.1007/s11665-017-2635-5

19. Todaka, T., Shimizu, K., Kusumoto, K., Purba, R.H., Gaqi, Y.: Effect of carbon content on three-body abrasive wear characteristics of 28Cr-3Ni cast alloys. ISIJ Int. **61**, 2274–2283 (2021). https://doi.org/10.2355/isijinternational.isijint-2021-099

20. Dautzenberg, J.H., Zaat, J.H.: Quantitative determination of deformation by sliding wear. Wear **23**, 9–19 (1973). https://doi.org/10.1016/0043-1648(73)90036-7

21. Kirk, J.A., Swanson, T.D.: Subsurface effects during sliding wear. Wear **35**, 63–67 (1975). https://doi.org/10.1016/0043-1648(75)90142-8

22. Penagos, J.J., Ono, F., Albertin, E., Sinatora, A.: Structure refinement effect on two and three-body abrasion resistance of high chromium cast irons. Wear **340–341**, 19–24 (2015). https://doi.org/10.1016/j.wear.2015.03.020

23. Matsuo, T.T., Kiminami, C.S., Fo, W.J.B., Bolfarini, C.: Sliding wear of spray-formed high-chromium white cast iron alloys. Wear 445–452 (2005)

24. Sun, T., Song, R.B., Wang, X., Deng, P., Wu, C.J.: Abrasive wear behavior and mechanism of high chromium cast iron. J. Iron Steel Res. Int. **22**, 84–90 (2015). https://doi.org/10.1016/S1006-706X(15)60014-0

25. Asensio, J., Pero-Sanz, J.A., Verdeja, J.I.: Microstructure selection criteria for cast irons with more than 10 wt.% chromium for wear applications. Mater. Charact. **49**, 83–93 (2002). https://doi.org/10.1016/S1044-5803(02)00260-7

26. ASM International: ASM Handbook Volume 5: Surface Engineering. ASM International, Novelty, OH (2002)

27. Laird, G., Gundlach, R., Rohrig, K.: Abrasion-Resistant Cast Iron Handbook. American Foundry Society, Schaumburg, IL (USA) (2000)

28. Avery, H.S.: The measurement of wear resistance. Wear **4**, 427–449 (1961). https://doi.org/10.1016/0043-1648(61)90301-5

29. Fulcher, J.K., Kosel, T.H., Fiore, N.F.: The effect of carbide volume fraction on the low stress abrasion resistance of high Cr-Mo white cast irons. Wear **84**, 313–325 (1983). https://doi.org/10.1016/0043-1648(83)90272-7

30. Rodenburg, C., Rainforth, W.M.: A quantitative analysis of the influence of carbides size distributions on wear behaviour of high-speed steel in dry rolling/sliding contact. Acta Mater. **55**, 2443–2454 (2007). https://doi.org/10.1016/j.actamat.2006.11.039

31. Nayak, U.P., Mücklich, F., Guitar, M.A.: Time-dependant microstructural evolution and tribological behaviour of a 26 wt% Cr white cast iron subjected to a destabilization heat treatment. Met. Mater. Int. (2022). https://doi.org/10.1007/s12540-022-01276-8

32. Nayak, U.P., Webel, J., Pesnel, V., Mücklich, F., Guitar, M.A.: Development of a protective coating for evaluating the subsurface microstructure of a worn material. Tribol. Lett. **69**, 1–13 (2021). https://doi.org/10.1007/s11249-021-01541-8

33. Nayak, U.P., Guitar, M.A., Mücklich, F.: Evaluation of etching process parameter optimization in the objective specific microstructural characterization of as-cast and heat treated HCCI alloy. Praktische Metallographie/Pract. Metall.. **57**, 688–713 (2020). https://doi.org/10.3139/147.110682

34. Oliver, W.C., Pharr, G.M.: An improved technique for determining hardness and elastic modulus using load and displacement sensing indentation experiments. J. Mater. Res. **7**, 1564–1583 (2011). https://doi.org/10.1557/JMR.1992.1564

35. Oliver, W.C., Pharr, G.M.: Measurement of hardness and elastic modulus by instrumented indentation: advances in understanding and refinements to methodology. J. Mater. Res. **19**, 3–20 (2004). https://doi.org/10.1557/JMR.2004.19.1.3

36. Nayak, U.P., Suárez, S., Pesnel, V., Mücklich, F., Guitar, M.A.: Load dependent microstructural evolution in an as-cast 26% Cr high chromium cast iron during unlubricated sliding. Friction. **10**, 1258–1275 (2022). https://doi.org/10.1007/s40544-021-0553-x

37. Inoue, A., Masumoto, T.: Carbide reactions (M3C→M7C3→M23C6→M6C) during tempering of rapidly solidified high carbon Cr-W and Cr-Mo steels. Metall. Trans. A **11**, 739–747 (1980). https://doi.org/10.1007/BF02661203

38. Vardavoulias, M., Papadimitriou, G., Pantelis, D.: Effect of M7C3→M23C6 transformation on fracture behaviour of cast ferritic stainless steels. Mater. Sci. Technol. **9**, 711–717 (1993). https://doi.org/10.1179/MST.1993.9.8.711

39. Wang, K., Li, D.: Formation of core (M7C3)-shell (M23C6) structured carbides in white cast irons: a thermo-kinetic analysis. Comput. Mater. Sci. **154**, 111–121 (2018). https://doi.org/10.1016/j.commatsci.2018.07.032

40. Archard, J.F.: Contact and rubbing of flat surfaces. J. Appl. Phys. **24**, 981–988 (1953). https://doi.org/10.1063/1.1721448

41. Oberle, T.L.: Wear of metals. JOM. **3**, 438–439 (1951). https://doi.org/10.1007/BF03397325

42. Roa, J.J., Fargas, G., Mateo, A., Jiménez-Piqué, E.: Dependence of nanoindentation hardness with crystallographic orientation of austenite grains in metastable stainless steels. Mater. Sci. Eng. A **645**, 188–195 (2015). https://doi.org/10.1016/j.msea.2015.07.096

43. Leyland, A., Matthews, A.: On the significance of the H/E ratio in wear control: a nanocomposite coating approach to optimised tribological behaviour. Wear **246**, 1–11 (2000). https://doi.org/10.1016/S0043-1648(00)00488-9

44. Tsui, T.Y., Pharr, G.M., Oliver, W.C., Bhatia, C.S., White, R.L., Anders, S., Anders, A., Brown, I.G.: Nanoindentation and nano-scratching of hard carbon coatings for magnetic disks. MRS Online Proc. Library. **383**, 447–452 (2011). https://doi.org/10.1557/PROC-383-447

45. Chen, L., Persson, J., Ståhl, J.E., Zhou, J.M.: Nano-scratching resistance of high-chromium white cast iron and its correlation with wear of cBN tool in machining. J. Superhard Mater. **39**, 365–372 (2017). https://doi.org/10.3103/S1063457617050094

46. Coronado, J.J.: Effect of load and carbide orientation on abrasive wear resistance of white cast iron. Wear **270**, 823–827 (2011). https://doi.org/10.1016/j.wear.2011.02.009

47. Jokari-Sheshdeh, M., Ali, Y., Gallo, S.C., Lin, W., Gates, J.D.: Comparing the abrasion performance of NiHard-4 and high-Cr-Mo white cast irons: The effects of chemical composition and microstructure. Wear **492–493**, 204208 (2022). https://doi.org/10.1016/j.wear.2021.204208